Geophysical Prospecting EAGE EUROPEAN ASSOCIATION OF GEOSCIENTISTS & ENGINEERS

Geophysical Prospecting, 2018, **66**, 798–817 doi: 10.1111/1365-2478.12581

Complex resistivity of mineral rocks in the context of the generalised effective-medium theory of the induced polarisation effect

Michael S. Zhdanov[1,2], Vlad Burtman[1,2], Masashi Endo[2]* and Wei Lin[1]

[1]*Consortium for Electromagnetic Modeling and Inversion (CEMI), The University of Utah, Salt Lake City, UT 84112 USA, and* [2]*TechnoImaging, Salt Lake City, UT 84107 USA*

Received October 2016, revision accepted September 2017

ABSTRACT

This paper develops the generalised effective-medium theory of induced polarisation for rock models with elliptical grains and applies this theory to studying the complex resistivity of typical mineral rocks. We first demonstrate that the developed generalised effective-medium theory of induced polarisation model can correctly represent the induced polarisation phenomenon in multiphase artificial rock samples manufactured using pyrite and magnetite particles. We have also collected representative rock samples from the Cu–Au deposit in Mongolia and subjected them to mineralogical analysis using Quantitative Evaluation of Minerals by Scanning Electron Microscopy technology. The electrical properties of the same samples were determined using laboratory complex resistivity measurements. As a result, we have established relationships between the mineral composition of the rocks, determined using Quantitative Evaluation of Minerals by Scanning Electron Microscopy analysis, and the parameters of the generalised effective-medium theory of induced polarisation model defined from the laboratory measurements of the electrical properties of the rocks. These relationships open the possibility for remote estimation of types of mineralisation and for mineral discrimination using spectral induced polarization data.

Key words: Complex resistivity, Induced polarisation, Mineral rocks, Generalised effective-medium theory.

INTRODUCTION

One of the major problems in mineral exploration is the inability to reliably distinguish between economic mineral deposits and uneconomic mineralisation. While the mining industry uses many geophysical methods to locate mineral deposits, until recently, there was no reliable technology for identification and characterisation of mineral resources. In this paper, we address this problem by studying the complex conductivity of mineral rocks, which is manifested by the induced polarisation (IP) effect. Indeed, effective conductivity of rocks is not necessarily a constant and real number but may vary with frequency and be complex. There are several explanations for these properties of effective conductivity. Most often, they are explained by the physical–chemical polarisation effects of mineralised particles of the rock material and/or by membrane effects in the pores of reservoirs (Marshall and Madden 1959; Wait 1959; Luo and Zang 1998; Vanhala and Peltoniemi 1992). The polarisability effect is usually associated with the surface polarisation of the coatings of the grains. This surface polarisation can be related to an electrochemical charge transfer between the grains and the host medium (Wong 1979; Wong and Strangway 1981; Klein, Biegler and Hornet 1984). Surface polarisation is manifested by accumulating electric charges at the surface of the grain. A double layer of charges is created, which results in a voltage drop across the grain boundary (Wait 1982).

The physical–mathematical principles of the IP effect were originally formulated in the pioneering works of Wait (1959, 1982) and Sheinman (1969). However, the IP method

*E-mail: masashi@technoimaging.com

did not find wide application in mineral exploration until the 1970s with the work of Zonge (e.g., Zonge 1974; Zonge and Wynn 1975) and Pelton (Pelton 1977; Pelton *et al.* 1978). Significant contributions were also made by Kennecott research team between 1965 and 1977 (Nelson 1997).

Over the last 40 years, several conductivity relaxation models have been developed, which provided quantitative characterisation of electric charging phenomena, for example, the empirical Cole–Cole model (Cole and Cole, 1941; Pelton *et al.* 1978; Kemna 2000; Kamenetsky, Stettler and Trigubovich 2010), the electrochemical model of Ostrander and Zonge (1978), and the empirical models of Kavian, Slob and Mulder (2012) and Gurin *et al.* (2015). Multiple iterations of a mechanistic model to predict the complex resistivity response of soils and rocks containing metallic minerals have been published recently as well (e.g., Revil *et al.* 2013; Revil, Florsch and Mao 2015; Misra *et al.* 2016a,b).

Most of these developed models represent different aspects of IP phenomenon relatively well. In this paper, however, we will focus on the generalised effective-medium theory of the IP effect (GEMTIP) model, which uses the effective-medium theory to describe the complex resistivity of heterogeneous rocks (Zhdanov 2008a, b). It incorporates the physical and electrical characteristics of rocks at the porous/grain scale and translates them into an analytic expression for effective complex resistivity. These characteristics include grain size and conductivity, porous space shape, fluid and host rock conductivity values, porosity, anisotropy, polarisability, etc. It was shown in the papers by Zhdanov (2008a, b) that the widely accepted Cole–Cole model is a special case of the GEMTIP model, where all the grains have a spherical shape. In this paper, we investigate a more general case with the grains having an elliptical shape. By choosing different values of the ellipticity coefficient, one can consider oblate or prolate ellipsoidal inclusions, which provides a wide class of models to be used in the analysis of the complex conductivity of mineral rocks.

We first demonstrate in this paper that the GEMTIP model with elliptical inclusions can correctly represent the IP phenomenon in multiphase artificial rock samples. With the GEMTIP model, we have analysed the spectral IP responses of 35 artificial rock samples manufactured by Takakura *et al.* (2014) using pyrite and magnetite particles mixed with glass beads and a 0.01M KCl solution.

We have also applied the developed GEMTIP model to studying the complex resistivity of typical mineral rocks. We have collected several dozens of representative rock samples from the Cu–Au deposit in Mongolia. These rock samples were subjected to mineralogical analysis using Quantitative Evaluation of Minerals by Scanning Electron Microscopy (QEMSCan) technology (Rollinson *et al.* 2011). We have also conducted an analysis of the electrical properties of the same samples using the laboratory complex resistivity measurement system.

In order to invert the complex resistivity data for the GEMTIP model parameters, we have applied the hybrid method based on a genetic algorithm with simulated annealing and the regularised conjugate gradient method, SAAGA-RCG (Lin *et al.* 2015). The results of this study demonstrate that GEMTIP can correctly represent the IP phenomenon in the artificial and natural rock samples. We have also established relationships between the mineral composition of the rocks, determined using QEMScan analysis, and the parameters of the GEMTIP model defined from laboratory measurements of the electrical properties of the rocks. These relationships open the possibility for remote estimation of types of mineralisation using spectral IP data.

BASIC FORMULAS OF THE EFFECTIVE-MEDIUM THEORY OF INDUCED POLARISATION

It was demonstrated in Zhdanov (2008a,b, and 2010) that the induced polarisation (IP) phenomenon can be mathematically explained by a composite geoelectrical model of rock formations. This model is based on effective-medium theory, which takes into account the surface polarisation of grains and provides a more realistic representation of complex rock formations than conventional unimodal conductivity models.

A generalised effective-medium theory of the IP effect (GEMTIP), introduced in the cited papers, allows us to model the relationships between the physical characteristics of different types of rocks and minerals (e.g., conductivity values, grain sizes, porosity, anisotropy, and polarisability) and the parameters of the relaxation model. The GEMTIP model can be applied to examining the IP effect in complex rock formations composed of different mineral structures with varied electrical properties. In this section, for completeness, we will briefly review the basic principles of the generalised effective-medium approach as per the original paper by Zhdanov (2008a).

In the framework of the GEMTIP model, we represent a complex heterogeneous rock formation as a composite model formed by a homogeneous host medium of a volume V with a complex conductivity tensor $\widehat{\boldsymbol{\sigma}}_0$ filled with grains of arbitrary shape and conductivity. In the problem presented here, the rock is composed of a set of N different types of grains, with the lth grain type having a complex tensor conductivity tensor $\widehat{\boldsymbol{\sigma}}_l$. The grains of the lth type have a volume fraction f_l in the medium and a particular shape and orientation. Therefore, the total conductivity tensor of the model, i.e., $\widehat{\boldsymbol{\sigma}}(\mathbf{r})$ (where $\mathbf{r}$ is an observation point), has the following distribution for volume fraction f_l and volume fraction $f_0 = (1 - \sum_{l=1}^{N} f_l)$, respectively:

$$\widehat{\boldsymbol{\sigma}}(\mathbf{r}) = \begin{cases} \widehat{\boldsymbol{\sigma}}_0 \text{ for volume fraction } f_0 \\ \widehat{\boldsymbol{\sigma}}_l \text{ for volume fraction } f_l \,. \end{cases} \tag{1}$$

In order to find the effective conductivity tensor $\widehat{\boldsymbol{\sigma}}_e$, we represent the given inhomogeneous composite model as a superposition of a homogeneous infinite background medium with the conductivity tensor $\widehat{\boldsymbol{\sigma}}_b$ and the anomalous conductivity $\Delta\widehat{\boldsymbol{\sigma}}(\mathbf{r})$:

$$\widehat{\boldsymbol{\sigma}}(\mathbf{r}) = \widehat{\boldsymbol{\sigma}}_b + \Delta\widehat{\boldsymbol{\sigma}}(\mathbf{r}). \tag{2}$$

Following Zhdanov (2008a), we can write the following expression for the effective conductivity of the polarised inhomogeneous medium:

$$\widehat{\boldsymbol{\sigma}}_e = \widehat{\boldsymbol{\sigma}}_0 + \sum_{l=1}^{N} \left[\widehat{\mathbf{I}} + \widehat{\mathbf{p}}_l\right]^{-1} \left[\widehat{\mathbf{I}} - \Delta\widehat{\boldsymbol{\sigma}}_l^{p} \cdot \widehat{\Gamma}_l\right]^{-1} \cdot \left[\widehat{\mathbf{I}} + \widehat{\mathbf{p}}_l\right] \cdot \Delta\widehat{\boldsymbol{\sigma}}_l \, f_l, \tag{3}$$

where $\widehat{\boldsymbol{\sigma}}_e$ is an effective-medium complex conductivity tensor; $\Delta\widehat{\boldsymbol{\sigma}}_l$ is an anomalous conductivity tensor; $\Delta\widehat{\boldsymbol{\sigma}}_l^{p} = [\widehat{\mathbf{I}} + \widehat{\mathbf{p}}_l] \cdot \Delta\widehat{\boldsymbol{\sigma}}_l$ is the polarised anomalous complex conductivity; $\widehat{\mathbf{I}}$ is an identity tensor; $\widehat{\mathbf{p}}_l$ is a surface polarisability tensor; $\widehat{\Gamma}_l$ is a volume depolarisation tensor defined in Appendix A; and index l corresponds to the grain of the lth type. According to the definition (Zhdanov 2009, p. 524), the surface polarisability tensor $\widehat{\mathbf{p}}_l$ can be written as follows:

$$\widehat{\mathbf{p}}_l = \xi_l \widehat{\Gamma}_l^{-1} \cdot \widehat{\Lambda}_l, \tag{4}$$

where ξ_l is equal to

$$\xi_l = k_l \sigma_0 \sigma_l (\Delta\sigma_l)^{-1}, \tag{5}$$

$\Delta\sigma_l = \sigma_l - \sigma_0$ and k_l is a surface polarisability factor. The expressions for the volume $\widehat{\Gamma}_l$ and surface $\widehat{\Lambda}_l$ depolarisation tensors are given in Appendices A, B, and C.

It was shown by Wait (1982), Luo and Zang (1998), and Zhdanov (2008a) that the surface polarisability factor k_l is a complex function of frequency described by the following empirical model:

$$k_l = \beta_l (i\omega)^{-C_l}, \tag{6}$$

which fits the experimental data, where β_l is some empirical surface polarisability coefficient, measured in the units $[\beta_l] = \Omega\mathrm{m}^2/s^{C_l}$ and C_l is the relaxation parameter of the lth grain. The relaxation parameter (together with the time constant, which will be introduced later) determines the type of decreasing behaviour of the IP effect over time (in the time domain). For example, a larger value of relaxation parameter leads to steeper decrease in the IP effect over time (Kamenetsky *et al.* 2010). The physical meaning of these parameters will become more transparent when they will be presented in an equation of the GEMTIP resistivity relaxation model (11), developed subsequently, which could be treated as a generalisation of the widely used Cole–Cole model.

Formula (3) provides a general solution to the effective conductivity problem for an arbitrary multiphase composite polarised medium. This formula allows us to find the effective conductivity for inclusions with arbitrary shape and electrical properties. This is why the GEMTIP model can be used to construct effective conductivity for realistic rock formations typical for mineralisation zones and/or petroleum reservoirs; however, the calculation of the parameters of the GEMTIP model may become very complicated. It was demonstrated by Burtman and Zhdanov (2015) that there exists a special case of inclusions with ellipsoidal shape, where the solution of the GEMTIP formulas can be obtained in closed form, similar to a model with spherical inclusions. The advantage of the model with ellipsoidal inclusions is that, in this case, one can use different shapes of ellipsoids, from oblate to prolate, to model different types of heterogeneous rock formations and different types of inclusions. At the same time, for ellipsoidal geometry of the grains, the surface and volume depolarisation tensors, i.e., $\widehat{\Lambda}_l$ and $\widehat{\Gamma}_l$, can be calculated in closed form using the volume and surface integrals, as shown in Appendices B and C. Substituting the corresponding expressions for the surface and volume depolarisation tensors in equation (3), after some lengthy but straightforward algebra, we arrive at a general analytical solution for the principal components of the effective conductivity tensor of a multiphase composite anisotropic medium filled with ellipsoidal inclusions as follows:

$$\sigma_{e\alpha} = \sigma_0 + \sum_{l=1}^{N} (\sigma_l - \sigma_0) \, f_l \left[1 + \frac{\sigma_l - \sigma_0}{\sigma_0} \gamma_{l\alpha} + k_l \sigma_l \lambda_{l\alpha}\right]^{-1}, \quad \alpha = x, y, z. \tag{7}$$

where k_l is a surface polarisability factor introduced in equation (6) and $\gamma_{l\alpha}$ and $\lambda_{l\alpha}$ are scalar coefficients defined by geometrical parameters of the grains (see Appendices A, B, and C).

In particular, for the case of randomly oriented elliptical inclusions, the conductivity of the polarised inhomogeneous medium can be calculated by taking an average over the orientation in formula (7). As a result, we obtain the following formula for effective conductivity σ_e:

$$\sigma_e = \sigma_0 \left[1 + \frac{1}{3} \sum_{l=1}^{N} f_l D_l \right], \tag{8}$$

where

$$D_l = \sum_{\alpha=x,y,z} D_{l\alpha},$$

and

$$D_{l\alpha} = \frac{\rho_0 - \rho_l}{\rho_l + \gamma_{l\alpha} (\rho_0 - \rho_1) + k_l \lambda_{l\alpha}}. \tag{9}$$

The expression for the effective resistivity, $\rho_e = 1/\sigma_e$, of a medium filled with completely randomly oriented ellipsoidal grains can be written as follows:

$$\rho_e = \rho_0 \left[1 + \frac{1}{3} \sum_{l=1}^{N} f_l D_l \right]^{-1}. \tag{10}$$

It can be shown that, if the inclusions are conductive, $\rho_l \ll \rho_0$, then formula (10) is simplified as follows:

$$\rho_e = \rho_0 \left\{ 1 + \sum_{l=1}^{N} \frac{f_l}{3} \sum_{\alpha=x,y,z} \frac{1}{\gamma_{l\alpha}} \left[1 - \frac{1}{1 + s_{l\alpha} (i\omega\tau_l)^{C_l}} \right] \right\}^{-1}, \tag{11}$$

where ρ_0 is the DC resistivity of the host matrix, ω is the frequency, f_l is the fraction volume parameter, C_l is a relaxation parameter, and τ_l (in seconds) is the time constant of the lth grain, similar to the time constant of the Cole–Cole model. The time constant τ_l is related to the empirical surface polarisability coefficients β_l of expression (6) by the formula, similar to one introduced in the case of spherical grains (Zhdanov 2008a)

$$\tau_l = \left[\frac{\overline{a}_l}{2\beta_l} (2\rho_l + \rho_0) \right]^{1/C_l}, \tag{12}$$

where $\overline{a}_l$ is an average value of the equatorial (a_{lx} and a_{ly}) and polar (a_{lz}) radii of the ellipsoidal grains, i.e.,

$$\overline{a}_l = \frac{(a_{lx} + a_{ly} + a_{lz})}{3}. \tag{13}$$

In a case of the ellipsoid of revolution (spheroid), the equatorial radii are equal, $a_{lx} = a_{ly} = a_l$, and expression (13) takes the following form:

$$\overline{a}_l = \frac{(2a_l + \varepsilon a_l)}{3} = \frac{(2 + \varepsilon)}{3} a_l, \tag{14}$$

where $\varepsilon = a_{lz}/a_l$ is *an ellipticity* of the ellipsoid of revolution (spheroid).

As we noted above, the relaxation parameter, together with the time constant, determines the behaviour of the IP effect over time (in the time domain). For example, an increase in the time constant results in shifting the IP effect in a later time (Kamenetsky *et al.* 2010).

The coefficients $s_{l\alpha}$ ($l = 1, 2, \ldots N$; $\alpha = x, y, z$) in expression (11) are the structural coefficients defined by the geometrical characteristics of the ellipsoidal inclusions used to approximate the grains

$$s_{l\alpha} = r_{l\alpha}/\overline{a}_l, \quad r_{l\alpha} = 2\frac{\gamma_{l\alpha}}{\lambda_{l\alpha}}, \tag{15}$$

where $\gamma_{l\alpha}$ and $\lambda_{l\alpha}$ are the diagonal components of the volume and surface depolarisation tensors described in Appendices B and C.

Note that, for spheroidal grains, the equatorial radii are equal to each other ($a_{lx} = a_{ly} = a_l$), the polar radius is denoted by b_l ($a_{lz} = b_l$), and the equation for $s_{l\alpha}$ takes the following form:

$$s_{l\alpha} = \frac{3}{2 + \varepsilon_l} r_{l\alpha}/a_l, \tag{16}$$

where ε_l is an ellipticity, $\varepsilon_l = b_l/a_l$, of the lth type of grains.

In the case of a two-phase composite model with spherical inclusions, formula (16) is simplified, and formula (11) transforms into an expression similar to Cole–Cole formula of complex resistivity (Pelton *et al.* 1978; Zhdanov 2008a).

Table 1 presents a list of parameters used in the multi-phase ellipsoidal GEMTIP model (11).

INVERSION FOR PARAMETERS OF THE GENERALISED EFFECTIVE-MEDIUM MODEL

An important question is how well the developed generalised effective-medium theory of induced polarisation (GEMTIP) model with elliptical grains could represent the actual complex resistivity of the rocks. In order to answer to this question, we formulate the inverse GEMTIP problem as follows.

We introduce a vector $\mathbf{m}$ of the unknown model parameters, $\mathbf{m} = [\rho_0, f_l, \tau_l, C_l, a_l, \varepsilon_l;\ l = 1, 2, ..N]$, and a vector $\mathbf{d}$ of the observed data (the values of the complex resistivity as a function of frequency), i.e., $\mathbf{d} = [\rho_e(\omega_1), \rho_e(\omega_2), \rho_e(\omega_3), \ldots ..\rho_e(\omega_n)]$.

Using these notations, we can write expression (11) in the following form:

$$\mathbf{d} = A_G(\mathbf{m}), \tag{17}$$

where A_G is a forward modelling operator described by equation (11).

Table 1 List of parameters of the multiphase ellipsoidal GEMTIP model. ($l = 1, 2, \ldots N$)

Parameter	Name	Units	Description
ρ_e	effective resistivity	Ωm	resulting effective resistivity
ρ_0	matrix resistivity	Ωm	matrix resistivity of rock
f_l	grain volume fraction	m^3	volume fraction of the lth grain
a_l	grain equatorial radius	m	equatorial radius of the spheroid
b_l	grain polar radius	m	polar radius of the spheroid
ε_l	ellipticity	–	$\varepsilon_l = b_l/a_l$
ε_{l_p}	eccentricity	–	$\varepsilon_{l_p}=\sqrt{1-a_l^2/b_l^2}$ (prolate spheroid: $b_l > a_l$)
ε_{l_o}	eccentricity	–	$\varepsilon_{l_o}=\sqrt{a_l^2/b_l^2-1}$ (oblate spheroid: $b_l < a_l$)
τ_l	time constant	sec	time constant of the lth grain
C_l	relaxation parameters	–	decay coefficient
ω	angular frequency	sec^{-1}	EM angular frequency
β_l	surface polarisability coefficient	$(\Omega \times m^2)/s^{C_l}$	empirical coefficient
$\gamma_{l\alpha}$	structural parameter	–	function of ellipticity ε_l
$\lambda_{l\alpha}$	structural parameter	–	function of ellipticity ε_l
$r_{l\alpha}$	structural parameter	–	$r_{l\alpha} = 2\frac{\gamma_{l\alpha}}{\lambda_{l\alpha}}$
$s_{l\alpha}$	structural parameter	–	$s_{l\alpha} = \frac{3}{2+\varepsilon_l} r_{l\alpha}/a_l$

In order to find the parameters of the GEMTIP model, we should solve equation (17) with respect to $\mathbf{m}$. The problem is an ill-posed one, which means that the solution can be nonunique and unstable. The conventional way to solve this ill-posed problem using the regularisation theory is based on substituting for inverse problem (17) the minimisation of the corresponding Tikhonov parametric functional (Zhdanov 2002):

$$P^{\alpha}(\mathbf{m}) = \left\| \mathbf{W}_d (A_G(\mathbf{m}) - \mathbf{d}) \right\|_{L_2}^2 + \alpha S(\mathbf{m}) = \min, \tag{18}$$

where $\mathbf{W}_d$ is the data-weighting matrix and α is a regularisation parameter.

The first term in equation (18) is a misfit functional,

$$\varphi(\mathbf{m}) = \left\| \mathbf{W}_d (A_G(\mathbf{m}) - \mathbf{d}) \right\|_{L_2}^2,$$

determined as a weighted least square norm of the difference between the observed and predicted data. The second term is a minimum-norm stabilising functional,

$$S_{MN}(\mathbf{m}) = \left\| \mathbf{W}_m (\mathbf{m} - \mathbf{m}_{\text{apr}}) \right\|_{L_2}^2,$$

where $\mathbf{W}_m$ is the weighting matrix of the model parameters and $\mathbf{m}_{\text{apr}}$ is some *a priori* model.

We should note that, in a case of the GEMTIP inversion, the misfit and parametric functionals may be characterised by having multiple local minima. In this situation, the conventional gradient-type minimisation algorithms (e.g., Zhdanov 2002, 2015) may not be suitable for solving this problem. In order to overcome these difficulties and to find the global minimum, Lin *et al.* (2015) developed a hybrid method based on a genetic algorithm with simulated annealing and the regularized conjugate gradient method (SAAGA-RCG). The SAAGA-RCG method is an iterative solver, which first generates the best solution from the possible solution set (a population) on each iteration using the genetic and annealing operations and then applies the regularised conjugate gradient method at the final stage of the inversion to make the solution converge to the global minimum. An interested reader can find a detailed description of the SAAGA-RCG method in the paper by Lin *et al.* (2015). We have applied this algorithm to minimise the Tikhonov parametric functional (18).

We subsequently summarise the major steps of the SAAGA-RCG algorithm.

(1) Search subspace and search interval

The search subspace is selected from the model parameter space by determining the lower and upper bounds of the model parameters. The search intervals for every scalar component m_i of vector $\mathbf{m}$ are divided into 2^{N_i} segments, where numbers N_i determine the total number of free parameters in the search subspace.

(2) Selection of initial population and individuals

A possible solution (called an individual) is randomly generated from the search subspaces for each GEMTIP parameter. Following the conventional technique of the genetic algorithm, each scalar parameter m_i is encoded into the

Table 2 List of artificial rock samples

Case	Weight content	Size of minerals	Size of glass beads
1	Pyrite: 1%, 3%, 5%, 10%, 15%, 20%	1.4–2.0 mm	1 mm
2	Pyrite: 1%, 3%, 5%, 10%, 15%, 20%	0.7–1.0 mm	1 mm
3	Pyrite: 1%, 3%, 5%, 10%, 15%, 20%	1.4–2.0 mm	0.05 mm
4	Pyrite: 1%, 3%, 5%, 10%	0.5–0.7 mm	0.05 mm
5	Magnetite: 1%, 3%, 5%, 10%, 15%, 20%	1.4–2.0 mm	1 mm
6	Magnetite: 1%, 3%, 5%, 10%, 15%, 20%	0.7–1.0 mm	1 mm
7	10% pyrite and 20% magnetite	1.4–2.0 mm	1 mm

binary number. Then, all the binary numbers for different scalar components of vector **m** are connected into a string to form a binary representation of each individual. The above steps are repeated Q times, obtaining Q individuals.

(3) Fitness function

The fitness function is defined by the following expression:

$$f(k) = 1/\sum_{l=1}^{Q} \exp\left[(\psi(k) - \psi(l))/2\sigma\right],$$

where $k = 1, 2, \ldots, Q$; $\psi(k) = P^{\alpha}(\mathbf{m}^{(k)})$ is the parametric functional for the individual $\mathbf{m}^{(k)}$; and σ is the standard deviation of $\psi(k)$ over the entire initial population. The regularisation parameter α is selected using the adaptive regularisation (Zhdanov 2002, 2015).

(4) Selection

The "roulette rule" is used to determine which individual should be selected. The chances are higher for individuals that have larger fitness values.

(5) Crossover and mutation

In the framework of the genetic algorithm method, a new population is produced from the initial population by crossover and mutation operations (Whitley 1994). It is well known that moderately large values of crossover probability and small values of mutation probability are essential for the successful work of the genetic algorithm method. We also apply the adaptive genetic algorithm by adjusting the probabilities of crossover and mutation in each iteration.

(6) Annealing operation

It is known that the convergence of the genetic algorithm could be very slow. To overcome this difficulty, we use the adaptive genetic algorithm combined with the simulated annealing method (Kirkpatrick, Gelatt and Vecchi 1983)

(7) Regularised conjugate gradient operation

The stopping criterion for the inversion is based on the condition that the misfit is smaller than a given threshold value δ^2. The advantage of this method is that it allows the user to find the global minimum even in the case of very complex behaviour of the parametric functional (18), which is observed in the case of GEMTIP inversion.

ANALYSIS OF THE INDUCED POLARISATION EFFECT FOR ARTIFICIAL ROCK SAMPLES

Artificial rock samples

The artificial rock samples assembled by Takakura *et al.* (2014) were composed of mineral grains, glass beads, and a 0.01M KCL solution. Six different two-phase sample sets, which included one type of mineral (pyrite or magnetite) only, and one three-phase sample, which included both pyrite and magnetite, were prepared (a total of seven sample sets/cases, as shown in Table 2). For the cases of two-phase sample sets, each sample set contained different weighted concentrations of minerals, either pyrite or magnetite. The weighted concentrations for sample sets #1, #2, #3, and #5 were 1%, 3%, 5%, 10%, 15%, and 20%, respectively. In sample set #4, the weighted concentrations were 1%, 3%, 5%, and 10%. The weighted concentrations of pyrite and magnetite in the three-phase sample set (sample set #7) were 10% and 20%, respectively. We have studied how the induced polarisation (IP) effect changed with (1) the type of minerals, (2) the concentration of minerals, (3) the size of the minerals, and (4) the size of the glass beads. Overall, 35 individual samples (34 two-phase samples and one three-phase sample) were prepared.

According to Takakura *et al.* (2014), 1% content weight corresponded to 4 g in mass, and the volume of the artificial rock was 192 cm^3. Considering that the densities of the pyrite and magnetite were 5 and 5.15 g/cm^3, respectively, we calculated the volume fraction (content volume) for the mineral particles in the rock samples. Table 3 shows the volume fractions of pyrite and magnetite for each content weight.

The complex resistivity data for artificial rock samples were measured by Dr. Takakura (National Institute of Advanced Industrial Science and Technology (AIST)). The

Table 3 List of contents of mineral particles in volume weight and volume fraction

Content	1%	3%	5%	10%	15%	20%
Weight (*g*)	4	12	20	40	60	80
Volume of pyrite	0.42%	1.25%	2.08%	4.17%	6.25%	8.33%
Volume of magnetite	0.40%	1.21%	2.02%	4.05%	6.07%	8.09%

details of the complex resistivity measurement were described in Takakura, Nakada and Murakami (2013) and Takakura *et al.* (2014). The authors of the cited papers used stainless plates as the current electrodes and Ag–AgCl receiver electrodes, which were tested carefully in order to avoid polarisation errors. Solartron 1260 Impedance Analyzer and 1287 Potentiostat/Galvanostat were used to measure the complex resistivity data, which were further analysed by a single sine correlation. According to Takakura *et al.* (2013, 2014), this method had the accuracy of 0.1% in amplitude and 0.1° in phase. Similar studies in the past were conducted by Gurin *et al.* (2013), Mahan, Redman and Strangway (1986), Slater, Choi and Wu (2005), Slater, Ntarlagiannis and Wishart (2006), and Hubbard *et al.* (2014).

Analysis of the induced polarisation effect for the two-phase artificial mineral rocks

We ran the inversion of complex resistivity data for all 34 two-phase samples (cases 1 to 6 in Table 2) using the SAAGA-RCG algorithm, outlined above, for two-phase generalised effective-medium theory of induced polarisation (GEMTIP) model, where one phase was represented by either pyrite or magnetite and another phase was represented by the glass beads and KCl (assumed as the matrix).

Figure 1 shows a comparison of the real and imaginary parts of the complex resistivity spectra of the artificial mineral rocks composed of pyrite particles (panels (a) and (b))

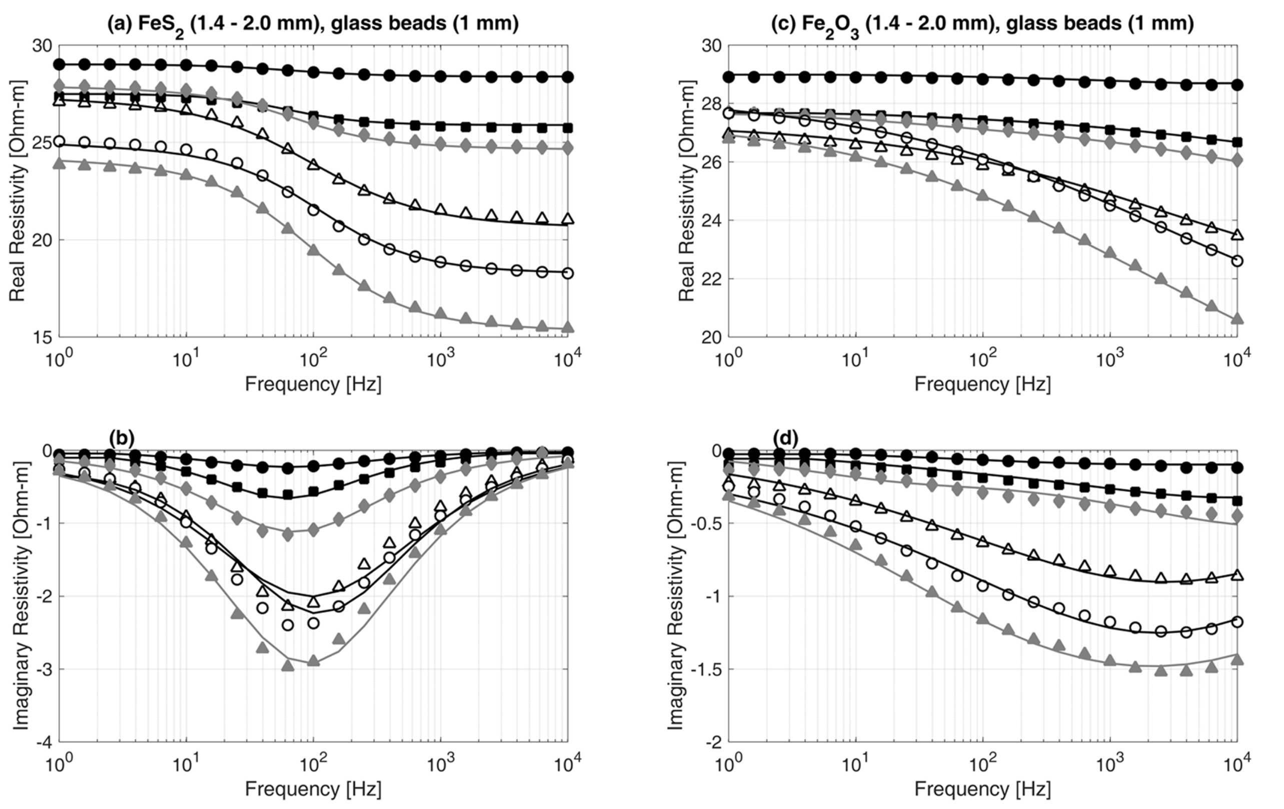

Figure 1 Observed and predicted complex resistivity spectra for artificial mineral rocks with pyrite (panels a and b) and magnetite (panels c and d) particles. The pyrite and magnetite particles are the same average size of 1.4–2 mm. The plots present the real (panels a and c) and imaginary (panels b and d) resistivities as functions of the frequency for six different mixing concentrations, 1%, 3%, 5%, 10%, 15%, and 20%, shown by bold dots, black squares, grey diamonds, triangulars, circles, and grey triangulars, respectively. The solid lines show the theoretical predicted complex resistivity curves based on the GEMTIP models.

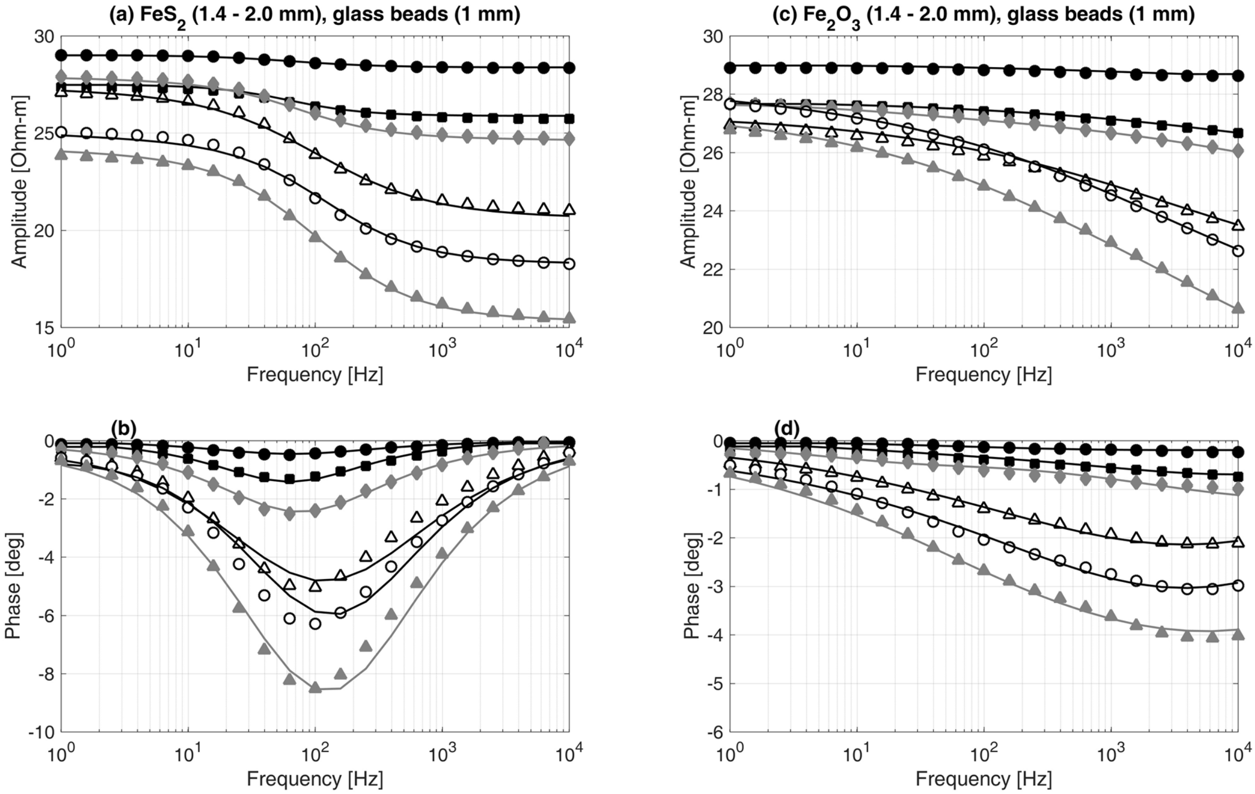

Figure 2 Observed and predicted complex resistivity spectra for artificial mineral rocks with pyrite (panels a and b) and magnetite (panels c and d) particles. The pyrite and magnetite particles are the same average size of 1.4–2 mm. The plots present the amplitude (panels a and c) and phase (panels b and d) resistivities as functions of the frequency for six different mixing concentrations, 1%, 3%, 5%, 10%, 15%, and 20%, shown by bold dots, black squares, grey diamonds, triangulars, circles, and grey triangulars, respectively. The solid lines show the theoretical predicted complex resistivity curves based on the GEMTIP models.

and magnetite particles (panels (c) and (d)) as examples. The pyrite and magnetite particles have the same average size of 1.4–2 mm, and the glass beads are of about 1 mm in size. The six measured complex resistivity spectra correspond to the six mixing concentrations, 1%, 3%, 5%, 10%, 15%, and 20%, shown by bold dots, black squares, grey diamonds, triangulars, circles, and grey triangulars, respectively. We used these experimental curves as input data in the solution to the GEMTIP inverse problem (17). The theoretical complex resistivity curves based on the GEMTIP model are shown by the solid lines for all experimental complex resistivity data. Panels (a) and (c) show the real parts of the complex resistivity; panels (b) and (d) present the imaginary parts of the complex resistivity. Figure 2 shows a comparison of the amplitude and phase of the complex resistivity data with the same dots and line styles as those used in Fig. 1. In this paper, we plot the complex resistivity data as real and imaginary resistivities instead of amplitude and phase because we invert the real and imaginary resistivities for the GEMTIP model parameters.

As an example, Table 4 shows the recovered GEMTIP parameters for two-phase artificial mineral rock for case 1 (1.4- and 2.0-mm grains of pyrite with 1-mm glass beads). We should note that ellipticity ε_1 is one of the very important factors to represent the observed complex resistivity data appropriately; in other words, we cannot fit the observed data if we assume the spherical grains (the two-phase GEMTIP model with spherical grain is equivalent to the Cole–Cole model).

Table 4 Recovered GEMTIP parameters for two-phase artificial mineral rocks for case 1 (1.4- and 2.0-mm grains of pyrite with 1-mm glass beads)

Content	1%	3%	5%	10%	15%	20%
ρ_0 $(\Omega \cdot m)$	29.1	27.6	28.0	27.3	25.2	24.0
$\varepsilon_1(-)$	3.37	3.10	3.50	4.42	3.84	4.41
τ_1 (s)	0.0024	0.0022	0.0015	0.0013	0.0012	0.0011
$C_1(-)$	0.81	0.82	0.81	0.80	0.81	0.81
f_1 (%)	0.45	1.29	2.08	4.16	6.20	8.32

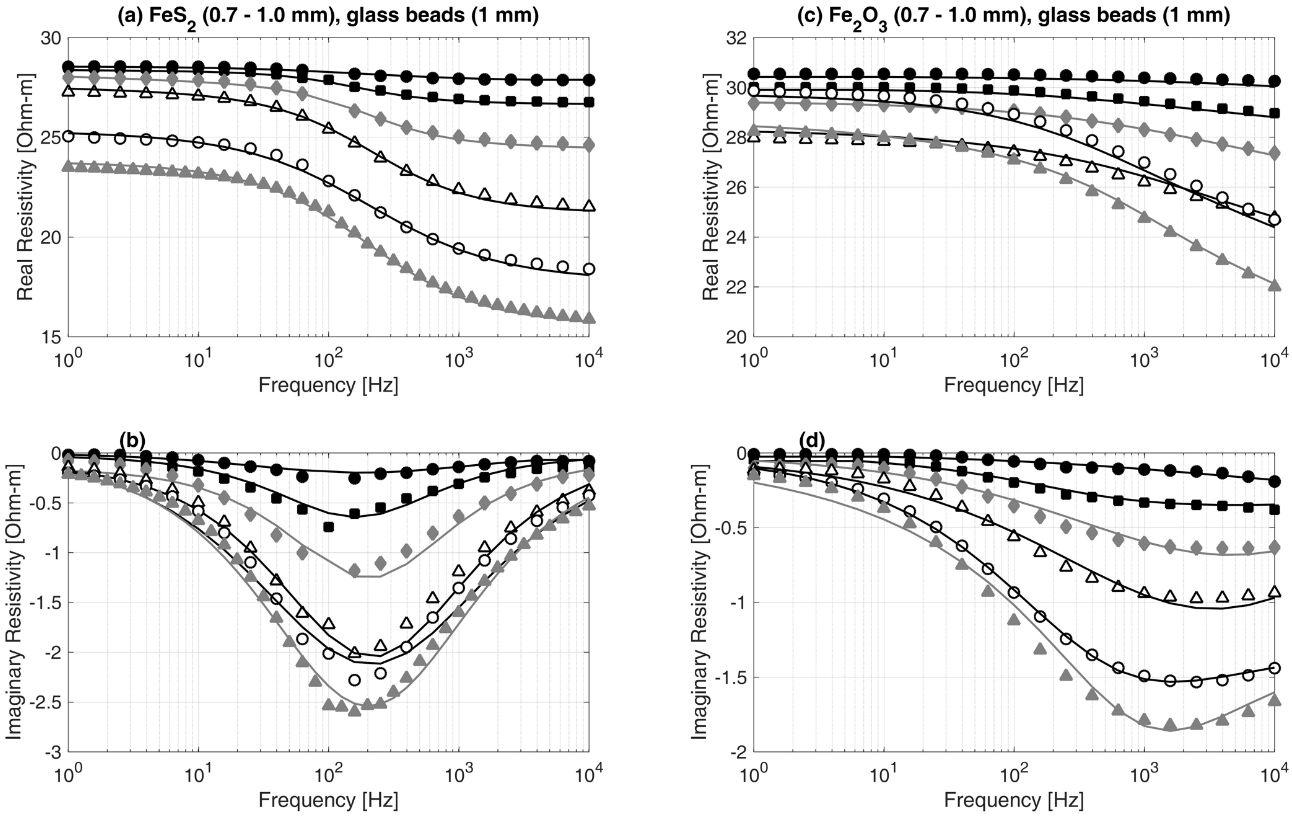

Figure 3 Observed and predicted complex resistivity spectra for artificial mineral rocks with pyrite (panels a and b) and magnetite (panels c and d) particles. The pyrite and magnetite particles have the same average size of 0.7–1 mm. The plots present the real (panels a and c) and imaginary (panels b and d) resistivities as functions of the frequency for six different mixing concentrations, 1%, 3%, 5%, 10%, 15%, and 20%, shown by bold dots, black squares, grey diamonds, triangulars, circles, and grey triangulars, respectively. The solid lines show the theoretical predicted complex resistivity curves based on the GEMTIP models.

The values of ellipticity in Table 4, recovered from GEMTIP inversion of the complex resistivity data, may indicate that the mineral particles in the artificial rock samples have ellipsoidal shape or they form clusters whose shape is ellipsoid.

Figure 3 also compares the complex resistivity spectra of the artificial mineral rocks composed of pyrite particles (panels (a) and (b)) and magnetite particles (panels (c) and (d)). However, the pyrite and magnetite particles are smaller, 0.7–1 mm, than in the previous case, and the glass beads have the same size of 1 mm. Similar to Fig. 1 , the six measured datasets of each spectrum correspond to the six mixing concentrations, 1%, 3%, 5%, 10%, 15%, and 20%, shown by bold dots, black squares, grey diamonds, triangulars, circles, and grey triangulars, respectively. The theoretical complex resistivity curves based on the GEMTIP inversion are shown by the solid lines for all experimental complex resistivity data. Panels (a) and (c) show the real parts of the complex resistivity; panels (b) and (d) present the imaginary parts of the complex resistivity. Note that all the inversions for two-phase sample sets (cases 1 to 6 in Table 2) converged quite well, and their final normalised misfit were less than 1%.

In order to analyse the IP properties of pyrite and magnetite, we plotted the content dependence of the time constant (τ), the relaxation parameter (C), and the matrix resistivity (ρ_0), recovered from GEMTIP inversions of complex resistivity data for all two-phase artificial rock samples (cases 1 to 6 in Table 2).

Figure 4 presents the plots of the time constant (τ) versus the content weight of the mineral particles for cases 1 to 6. For the pyrite particles (cases 1 to 4), the time constants are in a range of 4×10^{-4} to 5×10^{-3}, whereas for magnetite (cases 5 and 6), the range is of 5×10^{-6} to 1×10^{-4}. It is also clear from the produced plots that the mineral type, the size of the particles, and the content of the minerals are the major factors that affect the value of the time constant. For the particles of the same size (cases 1 and 5 or cases 2 and 6), the time constant

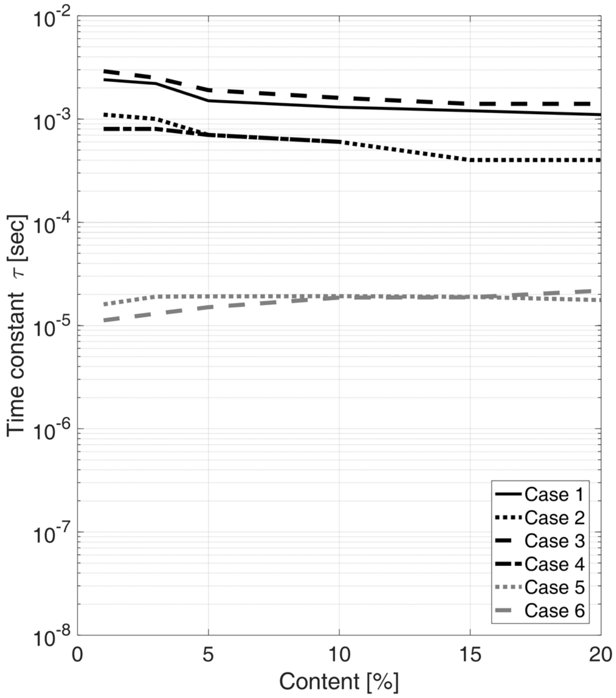

Figure 4 Time constant (τ) versus weight content of mineral particles for cases 1–6 using the GEMTIP model.

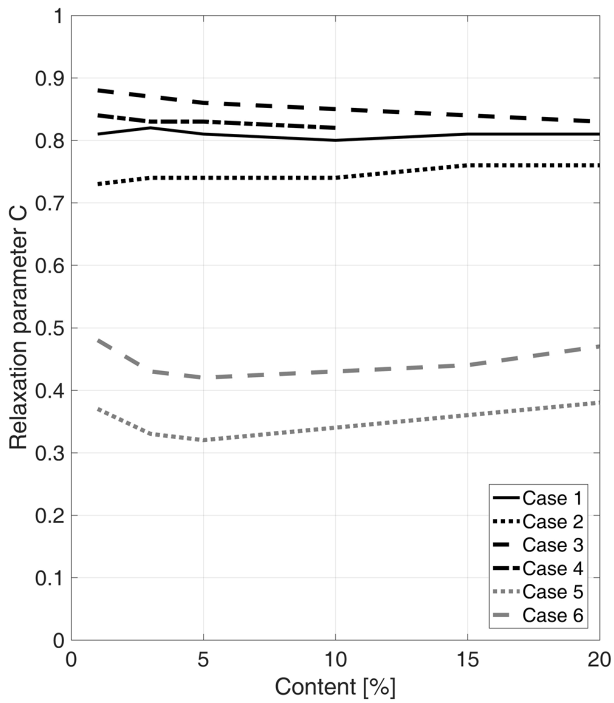

Figure 5 Relaxation parameter (C) versus weight content of mineral particles for cases 1–6 using the GEMTIP model.

for the pyrite sample is about 100 times larger than that for the magnetite sample.

In the case of the different sizes of pyrite, the artificial rock samples with the bigger particles tend to have a larger time constant. The time constant of the pyrite samples (ex. cases 3 and 4) decreases with the content of the particles increases in the range of 0−15%, and for larger content, the curve tends to be steady. In the case of the magnetite samples (cases 5 and 6), the time constant is much smaller than that for the pyrite samples, and it varies with the size very slowly. The difference in the time constants between the pyrite and magnetite samples may be due to the physical fact that pyrite is conductive and magnetite is resistive. As a result, the conductor (pyrite) requires more time to release the charges after the current cut-off during the measurement of the IP effect.

A comparison of recovered relaxation parameters (C) is shown in Fig. 5. The recovered relaxation parameters for both models show a similar behaviour. For the pyrite particles, the relaxation parameters are within the range of 0.7–0.9, whereas for magnetite, the range is within 0.3–0.5. From the inversion results, we can find that the relaxation parameter of the pyrite samples is affected by the size of the mineral particles and the glass beads. The artificial rock samples with the bigger pyrite particles and smaller glass beads tend to have larger C. In the case of the magnetite samples, the recovered relaxation parameters of the smaller magnetite particles are larger than those of the bigger particles. A comparison between the relaxation parameters for the pyrite and magnetite shows that the recovered C of the pyrite is less sensitive to the content of minerals. The relaxation parameter of the magnetite particles decreases within the range of 0%–5% and then increases within the range of 5%–20%. We should note that the uncertainty of complex resistivity measurement was 1–3 milliradian for the phase shift and 0.3% for amplitude measurement. Such uncertainties of complex resistivity measurement did not significantly affect the inversion results.

Figure 6 shows the matrix resistivity (ρ_0) versus the weight content of the minerals determined using the GEMTIP model. The matrix resistivity varies very slowly with the content of mineral particles. While it slightly decreases with the content of mineral particles in some cases (cases 1 and 2), we also observe a slight increase in the resistivity in case 3. One possible explanation of this phenomenon for case 3 could be related to the fact that the pyrite particles are characterised by very high surface impedances at lower frequencies, which we used in our measurements (see Yokoyama *et al.* 1984). It seems that the very small size of the glass beads used in case 3 (just 0.05 mm) could contribute to this effect as well.

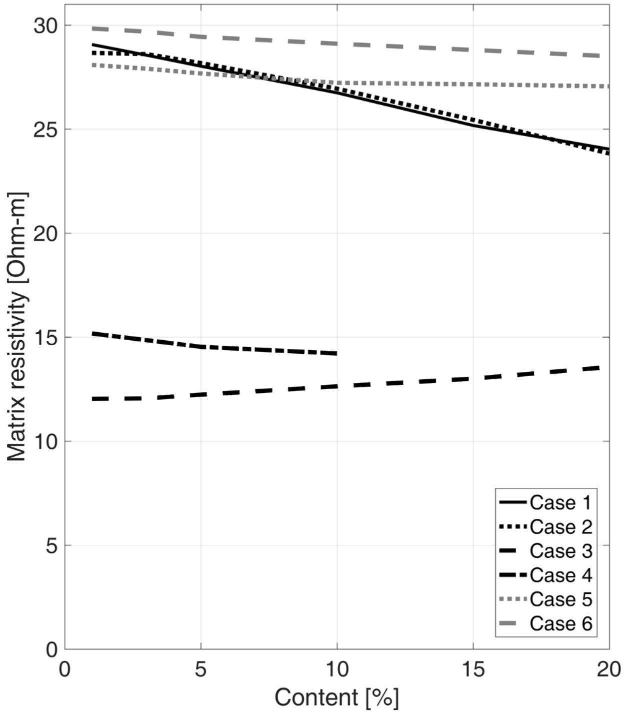

Figure 6 Matrix resistivity (ρ_0) versus weight content of mineral particles for cases 1–6 using the GEMTIP model.

More experimental study is needed to understand better this phenomenon, which was also observed by Revil *et al.* (2015).

Analysis of the induced polarisation effect for three-phase artificial mineral rocks

The last artificial rock sample (case 7) contains 10% pyrite and 20% magnetite (in weight), mixed with glass beads, which represents a three-phase medium. Takakura *et al.* (2014) describe that it is very difficult to discriminate the minerals (pyrite and magnetite) from the analysis of the complex resistivity spectra using the Cole–Cole model.

At the same time, by using the three-phase GEMTIP model (equation (11), with elliptical grains), we were able to successfully invert the complex resistivity data for this sample and determine the GEMTIP parameters for both pyrite and magnetite. For the comparison, we also inverted the same complex resistivity data using the three-phase GEMTIP model with spherical grains. Figure 7 shows a plot of the complex resistivity data predicted from two GEMTIP inversions (with elliptical and spherical grains) with observed complex resistivity data. Note that, for the case of the GEMTIP inversion with spherical grains, we have fixed the fraction volumes to the values recovered from the GEMTIP inversion with elliptical grains (these values are very close to the values calculated using volume weight, as shown in Table 3). Figure 7 demonstrates that the complex resistivity data predicted from the GEMTIP inversion with elliptical grains represent the observed complex resistivity data well, whereas the complex resistivity data predicted from GEMTIP inversion with spherical grain cannot fit the observed data. One can see in Table 5 that the recovered time constants ($\tau_1 = 1.40 \times 10^{-3}$, $\tau_2 = 8.01 \times 10^{-6}$) and relaxation parameters ($C_1 = 0.80$, $C_2 = 0.46$) of the pyrite and magnetite are within the ranges listed above, whereas time constants recovered from the GEMTIP inversion with spherical grains (Table 6) are not within the ranges listed above. These results demonstrate that ellipticity is one of the very important parameters to be used for an accurate representation of the complex resistivity data and that the GEMTIP model with elliptical grains can be used to distinguish between pyrite and magnetite in the analysed rock samples.

EXPERIMENTAL STUDY OF THE MINERAL ROCK SAMPLES

We will subsequently present the results of the QEMSCan and complex resistivity study of the rock samples from the Cu–Au deposit in Mongolia. The copper–gold ore is hosted in the hydrothermal alteration zone. The mineralisation is a low-sulfide type. The distribution of the mineralisation is uneven, and it was determined that the mineralisation is generally distributed in or in the vicinity of the quartz-carbonate gangue located inside of the hydrothermal alteration zone. Mineralisation is associated with chalcopyrite related to early quartz veins. The main exploration problem in this case is the ability to differentiate between normally barren pyrite-bearing alteration phases and mineralised chalcopyrite phases. Systems generally always have pyrite but not all are mineralised with Cu-bearing sulfides. Discrimination between pyrite and chalcopyrite could be considered as an important application of the induced polarisation (IP) survey.

Mineralogical analysis using the quantitative evaluation of minerals by scanning electron microscopy

The mineralogical analyses of mineral and host rock samples were performed using the quantitative evaluation of minerals by the scanning electron microscopy (QEMSCan) system, developed from the research pioneered by the Commonwealth Scientific and Industrial Research and Organisation (CSIRO)

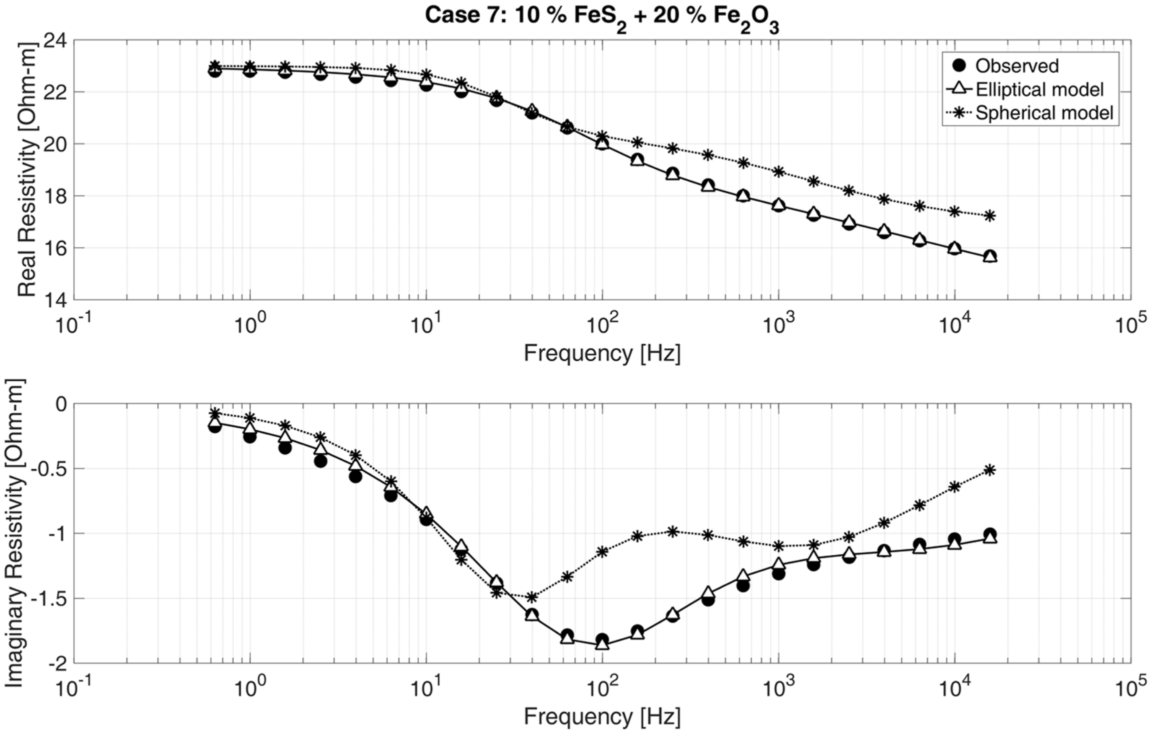

Figure 7 Plots of the observed and predicted complex resistivity data for case #7 (1.4- to 2.0-mm pyrite (10%) and magnetite (20%) with 1-mm glass beads). The white triangle dots with solid line show the complex resistivity data predicted from the GEMTIP inversion with elliptical grains, whereas the asterisk dots with dashed line show the complex resistivity data predicted from the GEMTIP inversion with spherical grains.

in Australia. QEMSCan combines features found in other analytical instruments such as a scanning electron microscope or electron probe micro-analyser into a next-generation solution designed for automated analysis of minerals, rocks, and materials. QEMSCan uses electron beam technology combined with high-resolution backscattered electron and secondary electron imaging and state-of-the-art energy-dispersive spectrometers to analyse minerals.

QEMSCan provides detailed particle mineralogical analysis, including quantification of mineral proportions, average grain size for selected mineral, average grain density, estimated minerals fraction volume, etc.

Rock samples were first cut in the middle to obtain a typical cross section. Following cutting, areas were marked on each sample for mounting as thin-film sections. The final QEMSCan images were used for determination of the fraction volume of different minerals. We should note that the mineralogical analysis of mineral proportions, average grain sizes for selected minerals, and estimated mineral volume fractions was based on the QEMSCan study of multiple parts of the thin sections of the rock samples in order to provide a statistically

Table 5 Inversion result for case #7 with elliptical GEMTIP model (10% and 20% of volume weight of pyrite and magnetite, respectively, mixed with glass beads)

$\rho_0(\Omega\text{m})$		23	
Mineral 1: Pyrite		Mineral 2: Magnetite	
e_1	3.6	e_2	4.2
τ_1 (*sec*)	1.40×10^{-3}	τ_2	8.01×10^{-6}
C_1	0.80	C_2	0.46
f_1, %	4.16	f_2, %	8.08

Table 6 Inversion result for case #7 with the spherical GEMTIP model (10% and 20% of volume weight of pyrite and magnetite, respectively, mixed with glass beads)

$\rho_0(\Omega\text{m})$		23	
Mineral 1: Pyrite		Mineral 2: Magnetite	
e_1	1	e_2	1
τ_1 (*sec*)	4.61×10^{-3}	τ_2	8.29×10^{-5}
C_1	1.00	C_2	0.67
f_1, %	4.16	f_2, %	8.08

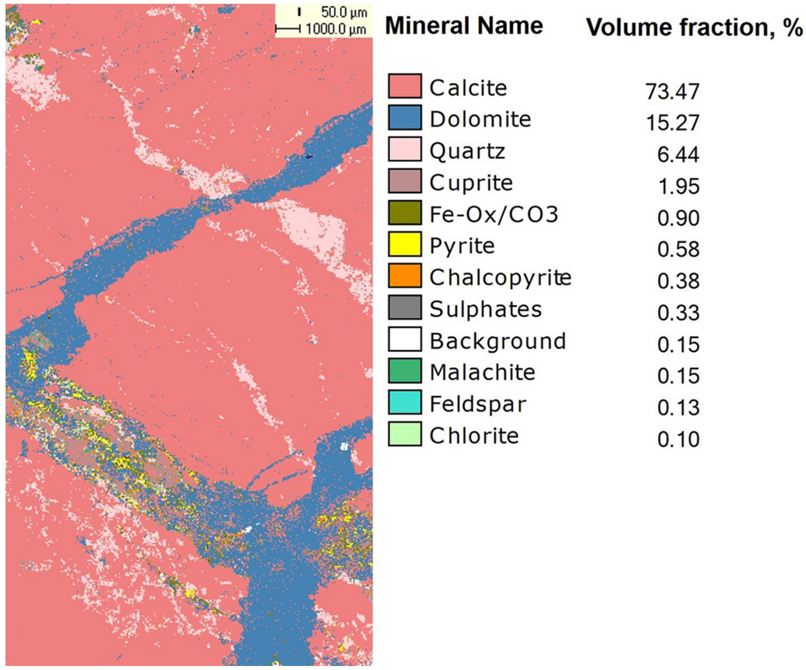

Figure 8 A QEMSCan image of rock sample #40 from the Au–Cu deposit, with a phase analysis shown on the right. Calcite and quartz are designated by the dark and light pink colours, respectively, whereas dolomite is shown by blue, chalcopyrite by orange, and pyrite by yellow in this image.

reliable mineralogical description of the entire sample, which could be used for a comparison with the generalised effective-medium theory of induced polarisation (GEMTIP) analysis. The images shown below represent just the examples of the QEMSCan analysis.

As an example, Figs. 8 and 9 present the typical images and the results of the QEMSCan analysis for rock samples #40 and #50.

Note that, according to the QEMSCan results, all samples contain more than one type of minerals. The major sulfide minerals present in these samples are chalcopyrite and pyrite. Therefore, in all these samples, we consider the structure that contains two different mineral phases and a host matrix phase, i.e., a total of three phases. Thus, the three-phase GEMTIP model was utilised for the analysis of complex resistivity.

Examples of the QEMSCan images of rock samples #40 and #50 from the Au–Cu deposit are shown in Figs. 8 and 9, with a phase analysis shown on the right. A QEMSCan image of rock sample #40 contains minerals shown in Fig. 8, with the major concentration of calcite (dark pink, matrix), dolomite (dark blue, veins), and quartz (light pink, veins), and there are some inclusions of pyrite (0.58%, yellow) and chalcopyrite (0.38%, orange). These sulfides are located in the proximity of dolomite veins.

A QEMSCan image of rock sample #50 (Fig. 9) contains quartz (light pink, veins) and feldspar (light green, matrix) with 2.64% of pyrite (yellow) and 0.15% of chalcopyrite (orange). The sulfides are located inside of quartz veins in this sample.

Measurements of complex resistivity and analysis of the induced polarisation effect

The system for measuring complex resistivity of the rock samples was developed based on our experience on working with Zonge International's complex resistivity system, which was used routinely for measuring the low-frequency (DC to 100 Hz) complex resistivity spectra of mineral rocks. In order to prevent the so-called spurious electrode polarisation effect at the electrode–sample interface, we used the non-polarised OYO electrodes; in addition, we placed the PVC cartridges, which were filled with distilled water between the electrodes to separate them. It was experimentally demonstrated that by using these modifications, the polarisation of the electrodes was within the instrumental error (Burtman, Gribenko and Zhdanov 2010; Burtman, Endo and Zhdanov 2011).

The complex resistivity measurement system operates in the frequency domain to avoid errors related to the conversion from the time domain to the frequency domain. The measurement setup contained two channels. We placed a rock core in one channel (called "test channel") and reference resistor R_{ref} in the other channel (called "reference channel"). The

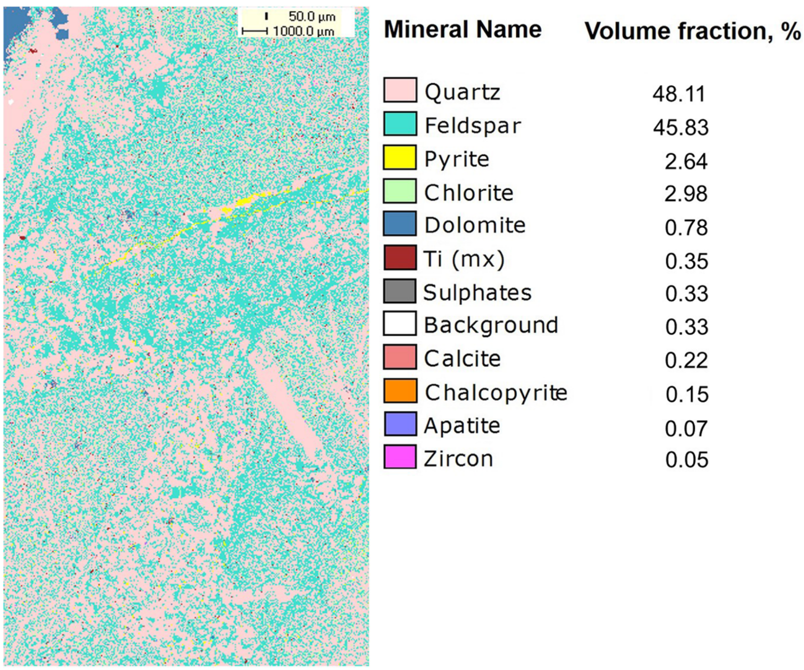

Figure 9 A QEMSCan image of rock sample #50 from the Au–Cu deposit, with a phase analysis shown on the right. Feldspar and quartz are designated by the dark green and light pink colours, respectively, whereas dolomite is shown by blue, chalcopyrite by orange, and pyrite by yellow in this image.

value of R_{ref} was selected to be approximately half of the core resistivity. We began complex resistivity measurement from a high frequency (e.g., 1 kHz) and then decreased the frequency to 0.01 Hz. During the complex resistivity measurements, the sin wave was generated using Agilent waveform generator (33521a) unit and sent through both the test and reference channels and recorded by Agilent two-channel digital Scope (dso-x-2012A) to evaluate the difference in amplitudes and phases between these two channels. The number of frequencies and the number of repeated measurements at each frequency could vary. The experimental results presented in this paper were based on using 36 frequencies and 3 repeated measurements per frequency to gain reliable complex resistivity data. We developed the LabVIEW program, which automatically applied the described measurement protocol and recorded the data. The amplitudes and phases of the recorded signals were examined by a spectrum analyser and converted into the real and imaginary parts of complex resistivity at each frequency. These individual complex resistivity measurements were then collated to form the complex resistivity spectrum of the sample. Additional experimental details of the complex resistivity measurement system can be found in Burtman *et al.* (2010 and 2011). To the best of our knowledge, our complex resistivity measurement system operates in a similar way as one that was recently independently developed by Prof. Lee Slater for Ontash & Ermac, Inc. (http://www.ontash.com/products.htm#PSIP)

Figures 10 and 11 show the real and imaginary parts of the complex resistivity spectra measured for the same samples #40 and #50, respectively. Remarkably, all the complex resistivity curves for the mineral rock samples are very similar to those for artificial rock sample, containing two minerals (Fig. 7). The major difference is that, in the case of the artificial rocks, those two minerals were pyrite and magnetite, whereas in the case of mineral rock samples #40 and #50, the IP generating minerals are pyrite and chalcopyrite. We can see also that the maximum IP response in the imaginary part of the complex resistivity curves (the minimum of the imaginary part) corresponds to a frequency of around 1 Hz in the case of mineral rock samples, whereas for the artificial rock sample, the negative "peak" in the imaginary part of the complex effective resistivity happens at a frequency of around 100 Hz. This shift of the frequency of the maximum IP response can be explained by a known fact that the peak in IP response tends to move to a higher frequency with the decrease in the size of the grains of the corresponding minerals (Ostrander and Zonge 1978; Zhdanov 2008a). The results of the QEMScan analysis show that the size of the pyrite grains varies within the range of 20–500 μm, whereas the chalcopyrite has small grains with a size less than 20 μm.

We have applied the inversion algorithm, SAAGA-RCG, to the observed complex resistivity data using a three-phase GEMTIP model. In this case, we have assumed, based on the results of the QEMScan analysis, that one phase was

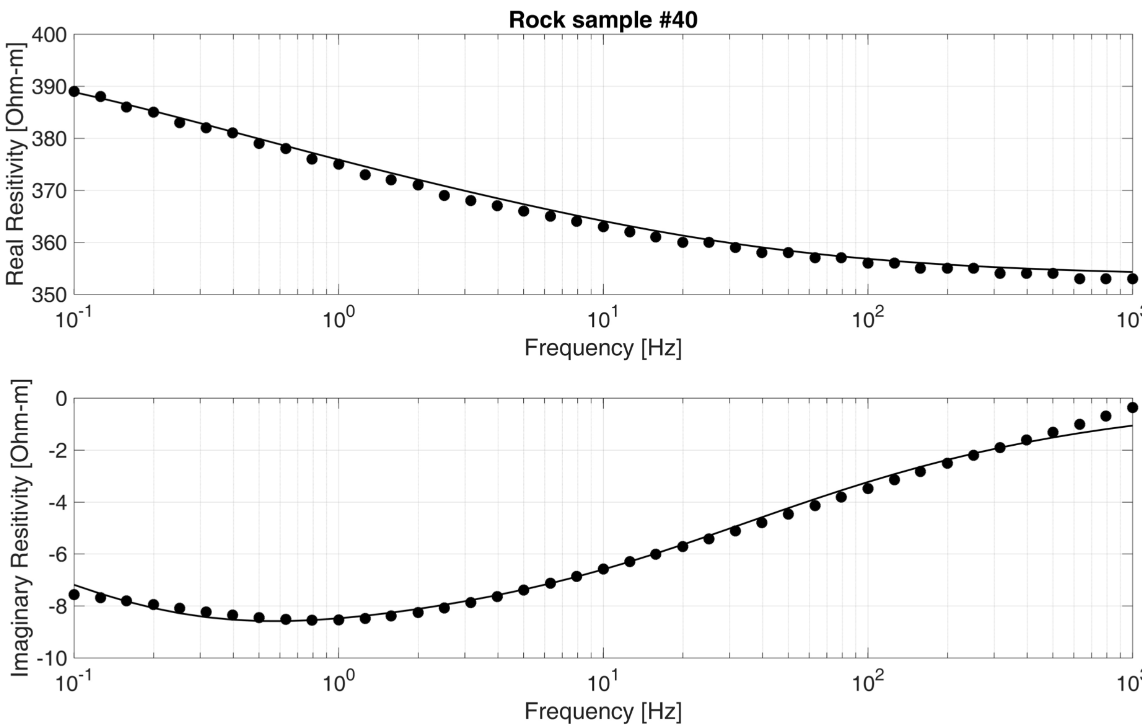

Figure 10 (Top panel) Real and (bottom panel) imaginary parts of (black dots) the observed complex resistivity spectrum and (black line) the data predicted based on the GEMTIP model for rock sample #40. The predicted data were obtained using the three-phase GEMTIP model.

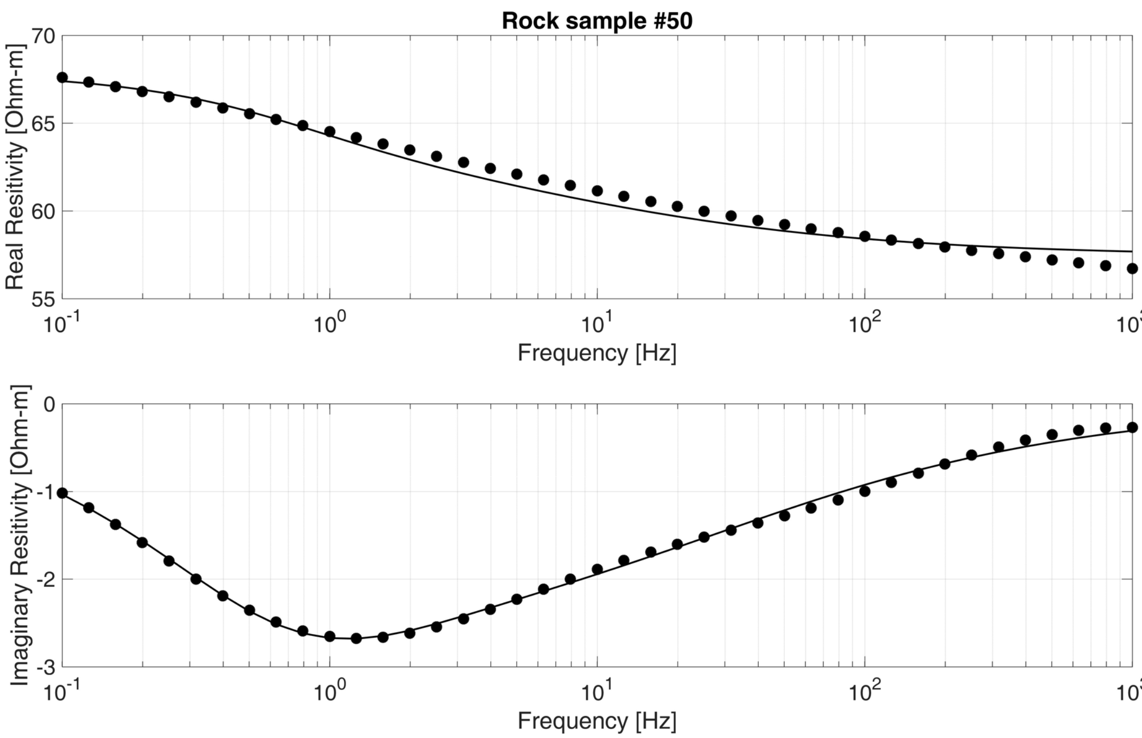

Figure 11 (Top panel) Real and (bottom panel) imaginary parts of (black dots) the observed complex resistivity spectrum and the data predicted based on (black line) the GEMTIP model for rock sample #50. The predicted data were obtained using the three-phase GEMTIP model.

Table 7 GEMTIP parameters for modelling of sample #40 from the Cu–Au deposit

$\rho_0(\Omega m)$		400	
Pyrite		Chalcopyrite	
e_1	6.6	e_2	9.6
τ_1 (s)	0.02	τ_2	0.55
C_1	0.57	C_2	0.55
f_1, %	0.51	f_2, %	0.46

represented by pyrite, another phase was represented by chalcopyrite, and the third phase was formed by other non-polarisable minerals. The predicted data obtained using the three-phase GEMTIP model are shown by the black lines in Figs. 10 and 11. Tables 5 and 6 present the corresponding GEMTIP parameters, produced by the inversion for samples #40 and #50, respectively. We should note that the values given in Tables 7 and 8 represent the parameters of the corresponding global minima determined by a SAAGA-RCG method.

The three-phase GEMTIP analysis of the real and imaginary parts of the complex resistivity spectrum (Fig. 10) of sample #40 demonstrates that the GEMTIP model correctly revealed the presence of two minerals, pyrite and chalcopyrite, in good agreement with the QEMSCan analysis of this sample (Fig. 8). The GEMTIP analyses provided larger values for the relaxation coefficient of pyrite grains than for chalcopyrite, and the time constant for pyrite was smaller than that for chalcopyrite. Therefore, the lower frequency minimum in Fig. 10 (top panel) is associated with pyrite, whereas the higher frequency increase is associated with chalcopyrite.

The three-phase GEMTIP analysis of the real and imaginary parts of the complex resistivity spectrum of sample #50 (Fig. 11) demonstrates that the GEMTIP model correctly represented the presence of pyrite in agreement with the QEMSCan analysis of this sample (Fig. 9). The GEMTIP analyses provided approximately the same values for the relaxation coefficient for the pyrite as for the chalcopyrite grains, whereas the chalcopyrite grains had larger time constant than the pyrite grains. Therefore, the lower frequency inflection point in Fig. 11 is associated with chalcopyrite, whereas the higher frequency increase is associated with pyrite.

We should note that the time constant and the relaxation parameters for pyrite, determined independently for two different rock samples, #40 and #50, are practically the same, which reflects the common properties of the pyrite's grains in both samples, taken from the same deposit. However, the shapes of the grains for two different rock samples, #40 and #50, are quite different, as one can see in Figs. 8 and 9. This difference in the shape is reflected in the different values of the recovered ellipticity. Chalcopyrite has a significantly larger time constant, which corresponds to relatively larger size of the grains.

Table 8 GEMTIP parameters for modelling of sample #50 from the Cu–Au deposit

$\rho_0(\Omega m)$		68	
Pyrite		Chalcopyrite	
e_1	3.0	e_2	7.5
τ_1 (s)	0.02	τ_2	0.18
C_1	0.56	C_2	0.88
f_1, %	2.78	f_2, %	0.49

DISCUSSION AND CONCLUSIONS

In this paper, we have analysed the generalised effective-medium theory of induced polarisation (GEMTIP) for the rock models with elliptical grains. This model is a generalisation of the classical Cole–Cole model, which appears in a special case of inclusions with spherical shape. The elliptical GEMTIP model provides analytical expressions connecting the effective electrical parameters of the rocks with the intrinsic petrophysical and geometrical characteristics of the composite medium: the mineralisation of the rocks, the matrix composition, and the polarisability of the formations.

We have successfully applied the new elliptical GEMTIP model to predict the IP effect in the artificial rock samples, formed by pyrite and magnetite particles mixed with glass beads, and inverted the experimental complex resistivity data observed in the artificial rock samples for the corresponding GEMTIP parameters. The inversion results indicate that the mineral type, the size of the particles, and the content of the minerals are the major factors that affected the time constant and relaxation parameters. Based on the inversion results of the complex resistivity data measured for the artificial rock samples, we have determined that the approximate range of the time constant for magnetite is 5×10^{-6} to 1×10^{-4} , whereas the time constant of pyrite decreases from 5×10^{-3} to 4×10^{-4} with the increase in the weight content of pyrite. The ranges of the relaxation parameter for pyrite and magnetite are 0.7–0.9 and 0.3–0.5, respectively. Therefore, it is possible to distinguish pyrite and magnetite from the observed complex resistivity data using the GEMTIP model.

Thus, we have experimentally demonstrated that the complex resistivity spectrum of the mineral rocks can be described well by a GEMTIP model with elliptical inclusions.

The results of the QEMSCan mineralogical, complex resistivity, and GEMTIP analysis of representative mineral rock samples collected from the Cu–Au deposit in Mongolia have shown that the elliptical GEMTIP model can be effectively used to model the IP effect in mineral rocks. Moreover, we have found that the different types of mineralisations are characterised by different behaviours of the parameters of the GEMTIP model. These results open the possibility for mineral discrimination based on complex resistivity measurements.

Future research should be focused on expanded experimental study of representative mineral rock samples from different mineral deposits using QEMSCan mineralogical analysis, complex resistivity measurements, and GEMTIP modelling and inversion.

ACKNOWLEDGEMENTS

The authors acknowledge the Consortium for Electromagnetic Modeling and Inversion (CEMI) and TechnoImaging for support of this research and permission to publish. They are thankful to Dr. Takakura and his colleagues for providing the results of the complex resistivity measurements for the artificial rock samples and to First Eurasian Mining LC for providing the mineral rock samples for petrophysical analysis.

They also acknowledge AMIRA and the sponsors of project P1058 for providing the support of the initial stages of their research on spectral induced polarisation effect in mineral rocks.

REFERENCES

Burtman V., Endo M. and Zhdanov M.S. 2011. High-frequency induced polarization measurements of hydrocarbon-bearing rocks. 81st SEG annual international meeting, Expanded Abstracts.

Burtman V., Gribenko A. and Zhdanov M.S. 2010. Advances in experimental research of induced polarization effect in reservoir rock. 80th SEG annual international meeting, Expanded Abstracts.

Burtman V. and Zhdanov M.S. 2015. Induced polarization effect in reservoir rocks and its modeling based on generalized effective-medium theory. *Resource-Efficient Technologies* **1**, 34–48.

Cole K.S. and Cole R.H. 1941. Dispersion and absorption in dielectrics. *Journal of Chemistry and Physics* **9**, 343–351.

Gurin G., Tarasov A., Ilyin Y. and Titov K. 2013. Time domain spectral induced polarization of disseminated electronic conductors: laboratory data analysis through the Debye decomposition approach. *Journal of Applied Geophysics* **98**, 44–53.

Gurin G., Titov K., Ilyin Y. and Tarasov A. 2015. Induced polarization of disseminated electronically conductive minerals: a semi-empirical model. *Geophysical Journal International* **200**, 1555–1565.

Hubbard C.G., West L.J., Rodriguez-Blanco J.D. and Shaw S. 2014. Laboratory study of spectral induced polarization responses of magnetite-Fe2+ redox reactions in porous media. *Geophysics* **79**, D21–D30.

Kamenetsky F.M., Stettler E.H. and Trigubovich G.M. 2010. *Transient Geoelectromagnetics*. Ludwig-Maximillian University of Munich.

Kavian M., Slob E.C. and Mulder W.A. 2012. A new empirical complex resistivity model. *Geophysics* **77**(3), E185–E191.

Kemna A. 2000. *Tomographic inversion of complex resistivity: theory and application*. PhD thesis. Ruhr University Bochum, Germany.

Kirkpatrick S.C., Gelatt D. and Vecchi M.P. 1983. Optimization by simulated annealing. *Science* **220**, 671–680.

Klein J.D., Biegler T. and Hornet M.D. 1984. Mineral interfacial processes in the method of induced polarization. *Geophysics* **49**, 1105–1114.

Landau L.D. and Lifshitz E.M. 1982. *Electrodynamics of the Continuous Medium*. 2nd edn. Elsevier Butterworse-Heinemann.

Lin W., Zhdanov M.S., Burtman V. and Gribenko A. 2015. GEMTIP inversion of complex resistivity data using a hybrid method based on a genetic algorithm with simulated annealing and regularized conjugate gradient method. 85th SEG annual international meeting, Expanded Abstracts.

Luo Y. and Zang G. 1998. *Theory and application of spectral-induced polarization*. Society of Exploration Geophysicists.

Mahan M.K., Redman J.D. and Strangway D.W. 1986. Complex resistivity of synthetic sulfide bearing rocks. *Geophysical Prospecting* **34**, 743–768.

Marshall D.J. and Madden T.R. 1959. Induced polarization, a study of its causes. *Geophysics* **24**, 790–816.

Misra S., Torres-VerdÃ-n C., Revil A., Rasmus J. and Homan D. 2016a. Interfacial polarization of disseminated conductive minerals in absence of redox-active species—Part 1: mechanistic model and validation. *Geophysics* **81**(2), E139–E157.

Misra S., Torres-Verdín C., Revil A., Rasmus J. and Homan D. 2016b. Interfacial polarization of disseminated conductive minerals in absence of redox-active species–Part 2: effective electrical conductivity and dielectric permittivity. *Geophysics* **81**(2), E159–E176.

Nelson P.H. 1997. Induced polarization research at Kennecott, 1965–1977. *The Leading Edge* **16**, 29–33.

Ostrander A.G. and Zonge K.L. 1978. Complex resistivity measurements of sulfide-bearing synthetic rocks. 48th SEG annual international meeting, Abstract M-6, 113.

Pelton W.H. 1977. *Interpretation of induced polarization and resistivity data*. PhD thesis, University of Utah, USA.

Pelton W.H., Ward J.G., Hallof J.G., Sill W.R. and Nelson P.H. 1978. Mineral discrimination and removal of inductive coupling with multifrequency IP. *Geophysics* **43**, 588–609.

Revil A., Woodruff W.F., Torres-Verdín C. and Prasad M. 2013. Complex conductivity tensor of anisotropic hydrocarbon-bearing shales andmudrocks. *Geophysics* **78**, D403–D418.

Revil A., Florsch N. and Mao D. 2015. Induced polarization response of porous media with metallic particles–Part 1: a theory for disseminated semiconductors. *Geophysics* **80**, D525–D538.

Rollinson G.K., Andersen J.C., Sticklanda R.J., Boni M. and Fairhurst R. 2011. Characterization of non-sulphide zinc deposits using QEMSCAN. *Minerals Engineering* **24**, 778–787.

Sheinman S.M. 1969. *Contemporary Physical Foundations of the Electrical Prospecting Theory*. Moscow, Russia: Nedra, 224pp.

Slater L., Choi J. and Wu Y. 2005. Electrical properties of iron-sand columns: implications for induced polarization investigation and performance monitoring of iron-wall barriers. *Geophysics* **70**, G87-G94.

Slater L., Ntarlagiannis D. and Wishart D. 2006. On the relationship between induced polarization and surface area in metal-sand and clay-sand mixtures. *Geophysics* **71**, A1-A6.

Stratton J.A. 1941. *Electromagnetic Theory*. New York: McGraw-Hill.

Takakura S., Nakada K. and Murakami H. 2013. Complex resistivity measurements of sericite. *Butsuri-Tansa* **66**(2), 119–125.

Takakura S., Sasaki Y., Takahashi T. and Matsukuma Y. 2014. Complex resistivity measurements of artificial samples containing pyrite and magnetite particles. *Butsuri-Tansa* **67**(4), 267–275.

Vanhala H. and Peltoniemi M. 1992. Spectral IP studies of Finnish ore prospects. *Geophysics* **57**, 1545–1555.

Wait J.R. 1959. The variable-frequency method. In: *Overvoltage Research and Geophysical Applications*, (ed. J.R. Wait). Pergamon.

Wait J.R. 1982. *Geo-Electromagnetism*, Academic Press.

Whitley D.L. 1994. A genetic algorithm tutorial, *Statistics and Computing* **4**, 65–85.

Wong J. 1979. An electrochemical model of the induced-polarization phenomenon in disseminated sulfide ores. *Geophysics* **44**, 1245–1265.

Wong J. and Strangway D.W. 1981. Induced polarization in disseminated rocks containing elongated mineralization sulfide ores. *Geophysics* **46**, 1258–1268.

Yokoyama H., Nakatsuka K., Abe M. and Kato S. 1984. Complex resistivity of artificial ore containing pyrite particles. *Butsuri-Tanko* **37**, 169–180.

Zhdanov M.S. 2002. *Geophysical Inverse Theory and Regularization Problems*. Elsevier, 628pp.

Zhdanov M.S. 2008a. Generalized effective-medium theory of induced polarization. *Geophysics* **73**, 197–211.

Zhdanov M.S. 2008b. New geophysical technique for mineral exploration and mineral discrimination based on electromagnetic methods. US Patent No. 7,324,899.

Zhdanov M.S. 2009. *Geophysical Electromagnetic Theory and Methods*. Elsevier, 848pp.

Zhdanov M.S. 2010. Electromagnetic geophysics: notes from the past and the road ahead. *Geophysics* **75**, 75A49–75A66.

Zhdanov M.S. 2015. Inverse theory and applications in geophysics. Elsevier, 704pp.

Zonge K. 1974. *Electrical properties of rocks as applied to geophysical prospecting*. PhD thesis, University of Arizona, USA.

Zonge K. and Wynn J.C. 1975. Recent advances and applications in complex resistivity measurements. *Geophysics* **40**, 851–864.

APPENDIX A: DEFINITION OF THE DEPOLARISATION TENSORS

Following Zhdanov (2008a), we introduce the volume $\widehat{\Gamma}$ and surface $\widehat{\Lambda}$ depolarisation tensors as follows:

$$\widehat{\Gamma} = \iiint_V \widehat{\mathbf{G}}_b\left(\mathbf{r} \mid \mathbf{r}'\right) dv', \tag{A1}$$

and

$$\widehat{\Lambda} = \iint_S \widehat{\mathbf{G}}_b\left(\mathbf{r} \mid \mathbf{r}'\right) \cdot \mathbf{n}\left(\mathbf{r}'\right) \mathbf{n}\left(\mathbf{r}'\right) ds', \tag{A2}$$

where V is the volume occupied by the grain, S is the surface of the grain, $\mathbf{n}(\mathbf{r}')$ is a unit vector of the outer normal to the surface S, and $\mathbf{n}(\mathbf{r}')\mathbf{n}(\mathbf{r}')$ denotes a dyadic product of two normal vectors.

Tensor function $\widehat{\mathbf{G}}_b(\mathbf{r} \mid \mathbf{r}')$ is a Green's tensor for the homogeneous anisotropic full space, which can be represented in the form of a dyadic Green's function:

$$\widehat{\mathbf{G}}_b\left(\mathbf{r} \mid \mathbf{r}'\right) = \nabla\nabla' g_b\left(\mathbf{r} \mid \mathbf{r}'\right),$$

where $\nabla\nabla'$ stands for a dyadic product of two operators ∇ and ∇'.

In the case of a quasi-static model of the field and isotropic homogeneous full space ($\widehat{\boldsymbol{\sigma}}_b = \widehat{\mathbf{I}}\sigma_b$):

$$g_b\left(\mathbf{r} \mid \mathbf{r}'\right) = \frac{1}{4\pi\sigma_b\left|\mathbf{r} - \mathbf{r}'\right|}. \tag{A3}$$

Note that the volume depolarisation tensor $\widehat{\Gamma}$ can be represented in the form of a surface integral as well. Indeed, according to the Gauss theorem, the volume depolarisation tensor $\widehat{\Gamma}$ is equal to

$$\widehat{\Gamma} = \iiint_V \widehat{\mathbf{G}}_b\left(\mathbf{r} \mid \mathbf{r}'\right) dv' = \iiint_V \nabla\nabla' g_b\left(\mathbf{r} \mid \mathbf{r}'\right) dv'$$

$$\nabla \iiint_V \nabla' g_b\left(\mathbf{r} \mid \mathbf{r}'\right) dv' = \nabla \iint_S g_b\left(\mathbf{r} \mid \mathbf{r}'\right) \mathbf{n}\left(\mathbf{r}'\right) ds'. \tag{A4}$$

APPENDIX B: CALCULATION OF THE VOLUME DEPOLARISATION TENSOR $\widehat{\Gamma}$ FOR AN ELLIPSOIDAL GRAIN

The volume depolarisation tensor $\widehat{\Gamma}$ of an ellipsoidal grain can be determined as (Stratton 1941; Landau and Lifshitz 1982, pp. 37-44) a diagonal tensor with the components equal to

$$\Gamma_{\alpha\alpha} = -\frac{a_x a_y a_z}{2\sigma_b} \int_0^\infty \frac{ds}{\left(s + a_\alpha\right) R_s} =$$

$$-\frac{3V}{8\pi\sigma_b} \int_0^\infty \frac{ds}{\left(s + a_\alpha\right) R_s} = -\frac{1}{\sigma_b}\gamma_\alpha, \tag{B1}$$

where a_x, a_y, and a_z are the semi-axes of the ellipsoidal grain; $V = 4\pi a_x a_y a_z/3$ is a volume of the ellipsoid; and γ_α are depolarisation factors:

$$\gamma_\alpha = \frac{3V}{8\pi}\int_0^\infty \frac{ds}{(s+a_\alpha)R_s}, \quad R_s = \sqrt{(s+a_x)(s+a_y)(s+a_z)}. \tag{B2}$$

Note that the depolarisation factors satisfy the following condition:

$$\gamma_x + \gamma_y + \gamma_z = 1. \tag{B3}$$

In particular, for a spherical grain, we immediately obtain the known result:

$$\Gamma_{xx} = \Gamma_{yy} = \Gamma_{zz} = -\frac{1}{3\sigma_b}. \tag{B4}$$

For a cylindrical inclusion with the axis parallel to the z-axis ($a_z \to \infty$), we have

$$\Gamma_{zz} = 0,\ \Gamma_{xx} = \Gamma_{yy} = -\frac{1}{2\sigma_b}. \tag{B5}$$

In the case of the inclusion represented by the flat horizontal thin sheet ($a_x, a_y \to \infty$), one can find

$$\Gamma_{xx} = \Gamma_{yy} = 0,\ \Gamma_{zz} = -\frac{1}{\sigma_b}. \tag{B6}$$

Note that, for ellipsoids of revolution (spheroidal-shaped particles) with the z-axis aligned with the axis of revolution of the ellipsoid, the horizontal semi-axes of the ellipsoid are equal ($a_x = a_y = a$, and $a_z = b$). In this case, the elliptical integrals in equation (B1) can be expressed by analytical functions (Landau and Lifshitz 1982, pp. 37-44), with

$$\gamma_z = \gamma,\ \gamma_x = \gamma_y = \frac{1}{2}(1-\gamma) \tag{B7}$$

and

$$\Gamma_{zz} = \Gamma = -\frac{\gamma}{\sigma_b},\ \Gamma_{xx} = \Gamma_{yy} = -\frac{1}{2\sigma_b}(1+\sigma_b\Gamma). \tag{B8}$$

The value of γ is determined by the eccentricity of a spheroid.

For example, in the case of the prolate spheroid ($b > a$) with $e = \sqrt{1 - a^2/b^2}$, we have

$$\gamma = \frac{1-e^2}{e^3}(\tanh^{-1} e - e). \tag{B9}$$

Note that, if $e \to 1$, the spheroid transforms into a long thin rod.

For the oblate spheroid ($b < a$), with eccentricity $e = \sqrt{a^2/b^2 - 1}$, we have

$$\gamma = \frac{1+e^2}{e^3}(e - \tan^{-1} e). \tag{B10}$$

APPENDIX C: CALCULATION OF THE SURFACE DEPOLARISATION TENSOR $\hat{\Lambda}$ FOR AN ELLIPSOIDAL GRAIN

Now let us calculate the surface depolarisation tensor for ellipsoidal grains. To simplify the calculations, we will consider the ellipsoids of revolution only. Introducing a system of coordinates x, y, z with the z-axis aligned with the axis of revolution of the ellipsoid, we represent the equation of the surface of the ellipsoid as

$$\frac{x^2}{a^2} + \frac{y^2}{a^2} + \frac{z^2}{b^2} = 1,$$

where $a = a_x = a_y$ and $b = a_z$ are the equatorial and polar radii of the ellipsoid, respectively.

In particular, we can write the equation for the surface of the ellipsoid in cylindrical coordinates (ρ, φ, z) as

$$x = \rho\cos\varphi;\quad y = \rho\sin\varphi;\quad \rho = (a/b)\sqrt{b^2 - z^2};\quad z \in [-b, b]. \tag{C1}$$

The expression for the surface depolarisation tensor (A2) in the centre of the ellipsoid ($\mathbf{r} = \mathbf{0}$) takes the following form:

$$\hat{\Lambda} = -\frac{a}{4\pi\sigma_b b^2}\int_0^{2\pi} d\varphi \int_{-b}^{b} \hat{\mathbf{g}}(\mathbf{r}')\cdot\hat{\mathbf{N}}(\mathbf{r}')Q(\mathbf{r}')dz', \tag{C2}$$

where

$$\hat{\mathbf{N}} = \mathbf{n}(\mathbf{r}')\mathbf{n}(\mathbf{r}') \tag{C3}$$

and

$$\hat{\mathbf{g}}(\mathbf{r}') = \nabla\nabla'\frac{1}{|\mathbf{r}'|}. \tag{C4}$$

Note that vector $\mathbf{n}(\mathbf{r}') = (n_x,\ n_y,\ n_z)$ is a unit vector normal to the ellipsoid

$$n_x = \frac{b\sqrt{b^2 - z'^2}}{Q}\cos\varphi;\ n_y = \frac{b\sqrt{b^2 - z'^2}}{Q}\sin\varphi;\ n_z = \frac{az'}{Q},$$
$$Q = \sqrt{b^4 - (b^2 - a^2)z'^2}.$$

Therefore, expression (C3) takes the following form:

$$\hat{\mathbf{N}} = \begin{pmatrix} n_x^2 & n_x n_y & n_x n_z \\ n_x n_y & n_y^2 & n_y n_z \\ n_x n_z & n_y n_z & n_z^2 \end{pmatrix} = \begin{pmatrix} n_{11} & n_{12} & n_{13} \\ n_{21} & n_{22} & n_{23} \\ n_{31} & n_{32} & n_{33} \end{pmatrix}, \tag{C5}$$

where the scalar components n_{ki} are calculated as

$$n_{11} = \frac{b^2(b^2 - z^2)}{Q^2}\cos^2\varphi;\; n_{12} = \frac{b^2(b^2 - z^2)}{Q^2}\sin\varphi\cos\varphi;$$

$$n_{13} = \frac{abz\sqrt{(b^2 - z^2)}}{Q^2}\cos\varphi;$$

$$n_{21} = \frac{b^2(b^2 - z^2)}{Q^2}\sin\varphi\cos\varphi;\; n_{22} = \frac{b^2(b^2 - z^2)}{Q^2}\sin^2\varphi;$$

$$n_{23} = \frac{abz\sqrt{(b^2 - z^2)}}{Q^2}\sin\varphi;$$

$$n_{31} = \frac{abz\sqrt{(b^2 - z^2)}}{Q^2}\cos\varphi;\; n_{32} = \frac{abz\sqrt{(b^2 - z^2)}}{Q^2}\sin\varphi;$$

$$n_{33} = \frac{a^2z^2}{Q^2};\; Q = \sqrt{b^4 - (b^2 - a^2)z^2}. \tag{C6}$$

We can write a similar matrix representation for tensor $\hat{\mathbf{g}}$

$$\hat{\mathbf{g}} = \begin{pmatrix} g_{11} & g_{12} & g_{13} \\ g_{21} & g_{22} & g_{23} \\ g_{31} & g_{32} & g_{33} \end{pmatrix}, \tag{C7}$$

where the scalar components g_{ij} are calculated as

$$g_{11} = \frac{b^3\left[3a^2(b^2 - z^2)\cos^2\varphi - R^2\right]}{R^5};$$

$$g_{11} = \frac{b^3\left[3a^2(b^2 - z^2)\sin^2\varphi - R^2\right]}{R^5};\, g_{33} = \frac{b^3[3b^2z^2 - R^2]}{R^5};$$

$$g_{12} = g_{21} = \frac{3a^2b^3(b^2 - z^2)}{R^5}\sin\varphi\cos\varphi;$$

$$g_{13} = g_{31} = \frac{3ab^4z\sqrt{b^2 - z^2}}{R^5}\cos\varphi;$$

$$g_{23} = g_{32} = \frac{3ab^4z\sqrt{b^2 - z^2}}{R^5}\sin\varphi;$$

$$R = \sqrt{a^2b^2 + (b^2 - a^2)z^2}. \tag{C8}$$

Substituting expressions (C3)–(C8) into formula (C2), after some algebra, we will find

$$\widehat{\Lambda} = -\frac{1}{\sigma_b}\begin{bmatrix} \lambda & 0 & 0 \\ 0 & \lambda & 0 \\ 0 & 0 & \lambda_z \end{bmatrix},$$

where

$$\lambda = \frac{ab^3}{2}\int_0^b \frac{[2a^2b^2 - (b^2 - a^2)z^2](b^2 - z^2)}{[a^2b^2 + (b^2 - a^2)z^2]^{5/2}\sqrt{b^4 - (b^2 - a^2)z^2}}dz \tag{C9}$$

and

$$\lambda_z = ba^3\int_0^b \frac{[3b^4 - b^2a^2 - (b^2 - a^2)z^2]z^2}{[a^2b^2 + (b^2 - a^2)z^2]^{5/2}\sqrt{b^4 - (b^2 - a^2)z^2}}dz. \tag{C10}$$

Note that, in the case of a spherical grain with a radius a,

$$\lambda = \lambda_z = \frac{2}{3a},$$

and the surface depolarisation tensor takes the following form:

$$\widehat{\Lambda} = -\frac{2}{3\sigma_b a}\widehat{\mathbf{I}}. \tag{C11}$$

In a general case of the ellipsoidal grains, one should numerically calculate integrals (C9) and (C10).

The surface depolarisation tensor for the spheroidal-shaped grains is equal to

$$\widehat{\Lambda}_l = -\frac{1}{\sigma_0}\begin{bmatrix} \lambda_l & 0 & 0 \\ 0 & \lambda_l & 0 \\ 0 & 0 & \lambda_{lz} \end{bmatrix},$$

where $\lambda_l = \lambda_{lx} = \lambda_{ly}$, and λ_{lz} can be calculated using integrals (C9) and (C10).